Changes in the Subduction of Southern Ocean Water Masses at the End of the Twenty-First Century in Eight IPCC Models

STEPHANIE M. DOWNES

Institute for Marine and Antarctic Studies, University of Tasmania, and Antarctic Climate and Ecosystems CRC, Hobart, Tasmania, Australia, and Program in Atmospheric and Oceanic Sciences, Princeton University, Princeton, New Jersey

NATHANIEL L. BINDOFF

Centre for Australian Weather and Climate Research, Aspendale, and Wealth from Oceans National Research Flagship, Clayton South, Victoria, and Institute of Marine and Antarctic Studies, University of Tasmania, and Antarctic Climate and Ecosystems CRC, Hobart, Tasmania, Australia

STEPHEN R. RINTOUL

Centre for Australian Weather and Climate Research, Aspendale, and Wealth from Oceans National Research Flagship, Clayton South, Victoria, and Antarctic Climate and Ecosystems CRC, Hobart, Tasmania, Australia

(Manuscript received 15 January 2010, in final form 23 August 2010)

ABSTRACT

A multimodel comparison method is used to assess the sensitivity of Subantarctic Mode Water (SAMW) and Antarctic Intermediate Water (AAIW) formation to climate change. For the Intergovernmental Panel on Climate Change A2 emissions scenario (where atmospheric CO_2 is 860 ppm at 2100), the models show cooling and freshening on density surfaces less than about 27.4 kg m^{-3}, a pattern that has been observed in the late twentieth century. SAMW (defined by the low potential vorticity layer) and AAIW (defined by the salinity minimum layer) warm and freshen as they shift to lighter density classes. Heat and freshwater fluxes at the ocean surface dominate the projected buoyancy gain at outcrop regions of SAMW and AAIW, whereas the net increase in the Ekman flux of heat and freshwater contributes to a lesser extent. This buoyancy gain, combined with shoaling of the winter mixed layer, reduces the volume of SAMW subducted into the ocean interior by a mean of 8 Sv (12%), and the subduction of AAIW decreases by a mean of 14 Sv (23%; 1 Sv $\equiv$ 10^6 m^3 s^{-1}). Decreases in the projected subduction of the key Southern Ocean upper-water masses imply a slow down in the Southern Ocean circulation in the future, driven by surface warming and freshening. A reduction in the subduction of intermediate waters implies a likely future decrease in the capacity of the Southern Ocean to sequester CO_2.

1. Introduction

The ocean takes up atmospheric CO_2 in the ventilation zones at mid and high latitudes, where the water masses are formed, and releases it in the equatorial upwelling regions (Takahashi et al. 2002). Observations and models estimate that about 40% of the global anthropogenic CO_2 uptake by the global ocean occurs south of 30°S (e.g., Orr et al. 2001; Sabine et al. 2004). However, less than 18% of the anthropogenic Southern Ocean CO_2 uptake is via high-latitude water masses aged more than 30 years (Sabine et al. 1999; McNeil et al. 2003), implying that the younger Subantarctic Mode Water (SAMW) and Antarctic Intermediate Water (AAIW) are the key water masses for Southern Ocean carbon uptake. These upper-limb water masses originate from subducting surface waters, which flow northward around the subtropical gyres and ventilate the thermocline. SAMW and AAIW carry surface properties into the ocean interior where they are progressively modified as they spread to other parts of the globe. SAMW has been used to trace anthropogenic signals of climate change (Banks et al. 2002), and both SAMW and AAIW absorb large quantities of anthropogenic CO_2 (Sabine et al. 2004). Changes in the rate of

Corresponding author address: Stephanie Downes, Princeton University, 300 Forrestal Road, Princeton, NJ 08544.
E-mail: sdownes@princeton.edu

DOI: 10.1175/2010JCLI3620.1

formation of mode and intermediate waters have the potential to alter the uptake and storage of CO_2 and heat in the Southern Ocean, with subsequent consequences for sea level rise, ocean heat content, and carbon uptake. However, the ventilation rates of these crucial water masses, and their sensitivity to change, remains uncertain. In this paper, we use output from coupled climate models forced with enhanced greenhouse gas forcing to diagnose how climate change will affect SAMW and AAIW formation and ventilation rates.

Water masses ventilate the ocean interior through the process of subduction. Southern Ocean subduction rates are largest in regions where the winter mixed layers are deep, such as the primary SAMW and AAIW formation zones, in the southeast Indian and Pacific basins (e.g., Karstensen and Quadfasel 2002a). In the literature, differences in observationally based and model estimates of subduction result from the use of differing wind stress climatologies, the inclusion or exclusion of eddy fluxes, the mixed layer depth criteria, and limited long-term annual hydrographic observations (e.g., Qiu and Huang 1995; Huang and Qiu 1998; Karstensen and Quadfasel 2002a). Karstensen and Quadfasel estimated the ventilation rate of mode waters in the Southern Hemisphere basins ranged between 21 and 44 Sv (Sv $\equiv 10^6$ m^3 s^{-1}) with the Ekman pumping into the thermocline and the lateral flux across the mixed layer base contributing equally. In the south Indian Ocean, Karstensen and Quadfasel (2002b) found that mode and intermediate water subduction was dominated by the lateral subduction term for densities greater than 25.2 and 27.3 kg m^{-3}, respectively. Using both observations and an analytical model, Huang and Qiu (1998) concluded that for densities less than 27.0 kg m^{-3} the South Pacific Ocean was ventilated at a rate of 21.6 Sv, with vertical subduction (Ekman pumping) the dominant mechanism. Using coupled ocean–atmosphere model output from the Intergovernmental Panel on Climate Change Fourth Assessment Report (IPCC AR4) (Meehl et al. 2009), we diagnose changes in the subduction of SAMW and AAIW as an equivalent volume transport.

The meridional fluxes of heat and freshwater provide a significant link between the Southern Ocean and the global ocean conveyor belt (Speich et al. 2004). However, their contribution to the formation of SAMW and AAIW remains under debate. Rintoul and England (2002) concluded that the observed SAMW temperature and salinity changes (between 1991 and 1996; i.e., with short time scales) were dominated by the Ekman transport of cold fresh surface waters across the Subantarctic Front (SAF) into the region of World Ocean Circulation Experiment hydrographic line SR3 south of Tasmania. They argue that the changes due to the increased surface heat fluxes and precipitation in the SAMW formation region were smaller than those from Ekman fluxes of heat and freshwater. On the other hand, model data and long-term observations, in the Indian sector along 32°S, indicate that increases in surface heat fluxes (and, to a lesser degree, precipitation) were mainly responsible for the cooling and freshening found at SAMW densities in the ocean interior (Banks and Bindoff 2003; Murray et al. 2007).

The majority of Coupled Model Intercomparison Project phase 3 (CMIP3) models used in Southern Ocean validation studies (e.g., Russell et al. 2006; Raphael and Holland 2006; Connolley and Bracegirdle 2007) have focused on comparisons of the mean climate over decadal or 20-yr periods, rather than changes in the climate. The IPCC Working Group 1 report (Solomon et al. 2007) concluded that the CMIP3 models simulate the broad features of past and present climates well. While the temporal change in sea surface temperature and wind stress has been assessed, few studies concentrate on the Southern Ocean. Sen Gupta et al. (2009) diagnosed changes in the Southern Ocean climate as projected by the IPCC AR4 models in the Special Report on Emissions Scenarios A1B at the end of the twenty-first century. They found that most of the 21 models assessed projected strengthening of the Southern Hemisphere westerlies, as well as a southward shift of the mean position of the westerlies and the ACC. Surface warming and freshening, and changes in Ekman transport, accounted for the shoaling of deep mixed layers and reduced winter sea ice. The results presented here also focus on changes in the Southern Ocean climate; however, particular attention is given to changes in the upper-ocean water masses as their properties change in the twenty-first century.

This study diagnoses the impacts of global warming on SAMW and AAIW, and is divided as follows. The next section describes the methodology for calculating changes in the properties of water masses using selected CMIP3 models. A comparison of modeled and observed trends in surface temperature and the freshwater flux and mean wind stress is presented in section 3, and the capacity of the eight IPCC models to realistically project changes in the subduction of SAMW and AAIW in the twenty-first century will be discussed. Section 4 presents an analysis of the model output for the SRES A2 projection and multimodel mean. The regional distribution and circumpolar average pattern of changes in the subduction rate and corresponding surface buoyancy forcings for SAMW and AAIW are described. The surface trends are linked with changes in temperature and salinity in the ocean interior. The paper ends with a summary and discussion of our main conclusions (section 5).

2. Models and methods

a. IPCC model output

Eight of the IPCC models were chosen for this study based on the availability of model output needed to calculate subduction and buoyancy forcing at the time of the analysis. Details of IPCC model output can be found on the Web site of the Program for Climate Model Diagnosis and Intercomparison (PCMDI; available online at http://www-pcmdi.llnl.gov/) and in Randall et al. (2007). The model's ocean grid resolution is given in Table 1. We examine the results from the individual models and from the multimodel mean (MMM). A MMM has often been found to provide a better estimate than any individual model owing to reduction of model error in the averaging process (Reichler and Kim 2008). To calculate the MMM, the ocean fields are linearly interpolated to a $1° \times 1°$ horizontal grid and to the 33 depth levels of Levitus (1982).

Following the approach of the IPCC AR4, we use two 20-yr periods. The initial period is the 1981–2000 mean run from the Twentieth-Century Climate in Coupled Model (20C3M) , based on atmospheric forcings from historical records. The atmospheric CO_2 is just above 380 ppm, and its rate of increase has risen from 1.6 (since 1980) to 2.1 (since 2000) ppm yr^{-1} (Arguez et al. 2007). We compare the 1981–2000 period to the 2081–2100 period from the A2 scenario, where the equivalent atmospheric CO_2 at 2100 is 860 ppm. A systematic drift from the initial state occurs in atmosphere–ocean general circulation models (AOGCMs) when the ocean slowly approaches an equilibrium state after coupling with other model components (Rahmstorf 1995; Dirmeyer 2001; Covey et al. 2006). A 150-yr linear trend of the IPCC preindustrial control runs (PIcntrl) with atmospheric CO_2 set at 290 ppm is used to remove the drift from the temperature, salinity, and velocity fields in the A2 projections in each model. Water masses subduct along density surfaces, so it is important to examine changes in the ocean properties on both density and pressure levels. Throughout this paper neutral density surfaces are referred to as "density surfaces," and potential temperature will be referred to as "temperature."

b. Subduction and buoyancy flux calculations

The decadal mean changes in the annual mean subduction rates S_{ann} are analyzed based upon the equations of Marshall et al. (1993, hereafter MNW):

$$S_{\text{ann}} = -\mathbf{u}_H \cdot \nabla H - w_H, \tag{1}$$

where $\mathbf{u}_H \cdot \nabla H$ represents the lateral induction given by the component of the horizontal northward and eastward velocities ($\mathbf{u}_H$) perpendicular to the tilted base of the winter mixed layer. The maximum winter mixed layer depth is denoted by H. A negative subduction rate represents fluid moving irreversibly into the mixed layer. We use a mixed layer depth density criterion of $|\rho_m - \rho_s| \leq 0.03$ kg m^{-3} in which ρ_m and ρ_s are the mixed layer and surface densities, respectively. This criterion has been found to be a reasonable measure of the mixed layer depth in the Southern Ocean in recent studies (e.g., Sallée et al. 2006; de Boyer Montégut et al. 2004; Dong et al. 2008). In the models where the downward vertical velocity has not been stored in the IPCC data archives, we use the approximation (three-dimensional continuity equation)

$$\frac{\partial w}{\partial z} = -\nabla \cdot \mathbf{U}, \tag{2}$$

where $\mathbf{U}$ represents the horizontal velocities. The climate models used to estimate subduction rates here do not resolve eddies; rather, the eddy contribution is parameterized and included in the IPCC velocity output. Eddies have been found to make a significant contribution to subduction in the Southern Ocean (Nurser et al. 1999; Naveira-Garabato et al. 2001; Sallée et al. 2010), but the eddy contribution is not estimated separately here.

MNW relate subduction to the net surface buoyancy flux, given by

$$\mathbf{B}_{\text{net}} = \frac{g\alpha}{C_w}\mathbf{H}_{\text{in}} - g\beta\overline{\rho}S_m(E - P) - \mathbf{B}_{\text{Ek}}, \tag{3}$$

where $\mathbf{H}_{\text{in}}$ is the net heat flux into the ocean (i.e., shortwave and longwave radiation and sensible and latent heat). The thermal expansion coefficient is given by α, and

TABLE 1. The eight IPCC models, the abbreviated names used in this paper, their meridional (lat) and zonal (lon) resolution, and the number of vertical depth levels (z). Note that the meridional resolution for the ECHO-G, MIROC(medres), and CM2.1 models increases toward the equator and that the number of depth levels refers to only the pressure levels and excludes the surface levels in sigma coordinates. The asterisk indicates the two models, CGCM3.1 and ECHO-G that contain heat and freshwater flux adjustments and excludes ozone forcing. Also indicated is whether a model output included the vertical velocity (w_o): in models that did not output w_o, it is approximated using Eq. (2).

Model	Abbreviation	Lat	Lon	z	w_o (Yes/No)
CCCMA CGCM3.1(T47)	CGCM3.1*	1.9	1.9	29	Yes
CSIRO Mk3.0	Mk3.0	0.84	1.87	31	Yes
CSIRO Mk3.5	Mk3.5	0.84	1.87	31	Yes
MIUB ECHO-G	ECHO-G*	0.5–2.8	2.8	20	No
GISS ModelE-R	GISS-ER	4	5	33	Yes
UKMO HadCM3	HadCM3	1.25	1.25	20	No
MIROC3.2 (medres)	MIROC (medres)	0.5–1.4	1.4	33	Yes
GFDL CM2.1	CM2.1	0.3–1	1	50	Yes

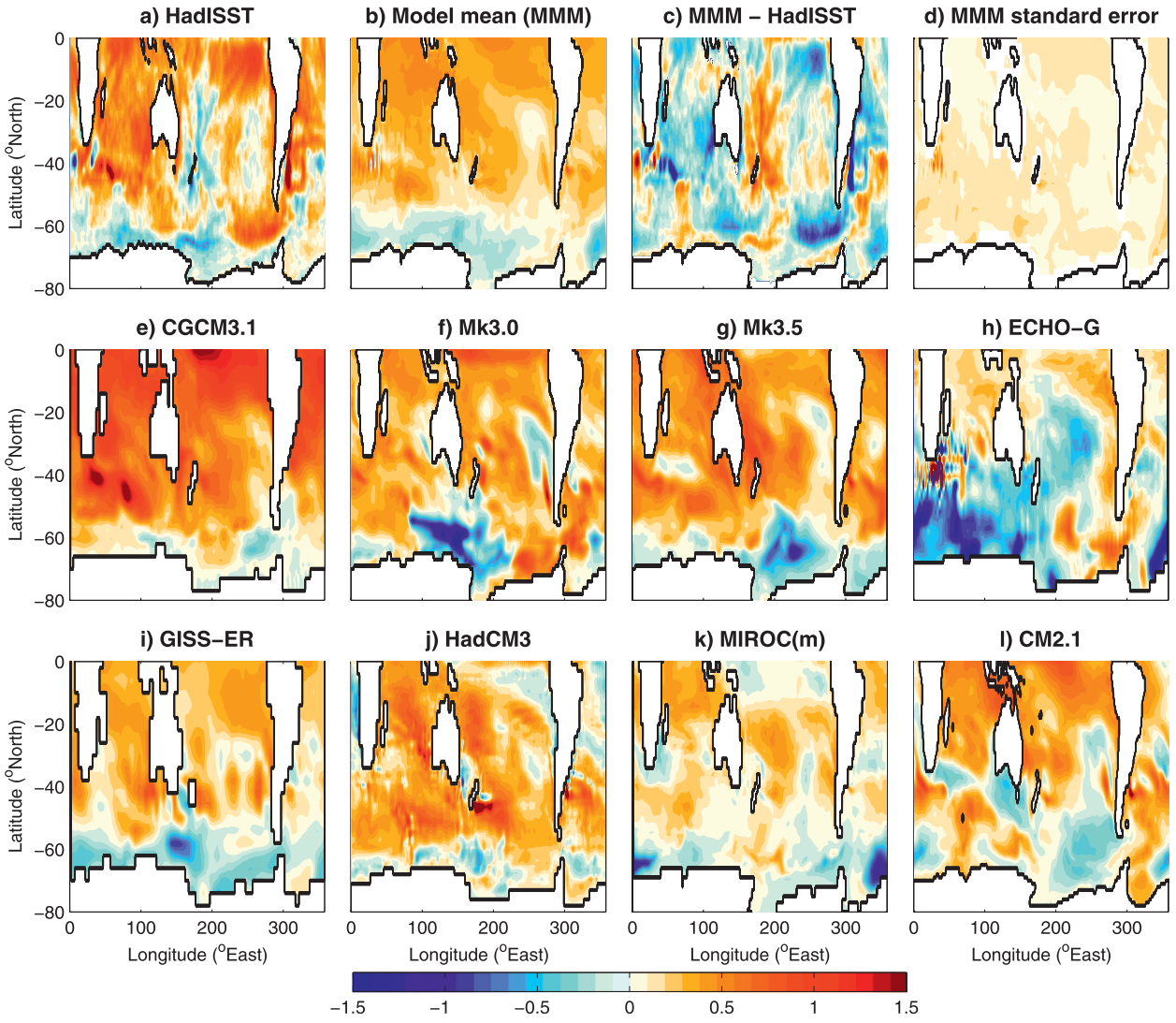

FIG. 1. Linear trend in SST shown as the difference in temperature (°C) for the period 1950–2000 in (a) the HadISST dataset (Rayner et al. 2003), (b) the MMM, (c) the difference between the MMM and HadISST, (d) the standard error in the MMM (i.e., std dev/$\sqrt{8}$), and (e)–(l) the CMIP3 models.

C_w is the heat capacity of water. The haline contraction coefficient is denoted by β, S_m is the salinity averaged over the mixed layer, g is the gravitational force, and the mean ocean density is given by $\overline{\rho}$. The freshwater flux is the difference between precipitation (P) and evaporation (E). We denote the air–sea fluxes as $\mathbf{B}_{\text{in}} = (g\alpha/Cw)\mathbf{H}_{\text{in}} - g\beta\overline{\rho}S_m(E-P)$ and the Ekman fluxes as $\mathbf{B}_{\text{Ek}}$. A positive $\mathbf{B}_{\text{net}}$ indicates buoyancy gain, that is, making the density of surface waters lighter due to surface warming and/or freshening.

The surface buoyancy added by the horizontal Ekman transport (MNW) is given by

$$\mathbf{B}_{\text{Ek}} = \frac{g}{\overline{\rho} f}\mathbf{k} \times \tau \cdot \nabla\rho_m. \tag{4}$$

The unit vertical vector is represented by $\mathbf{k}$, and ρ_m is the averaged mixed layer density.

3. Comparison of observed and modeled twentieth-century change

Heat and freshwater inputs influence the ocean density, and hence the mixed layer depth and the subduction rate [Eq. (1)]. We first compare the eight IPCC models to observed late twentieth-century SST and $P - E$ trends. The modeled and observed trends in SST between 1950 and 2000 are shown in Fig. 1. Warming of between 0.5° and 1°C was observed north of 45°S in the Met Office Hadley Centre Sea Ice and Sea Surface Temperature (HadISST) dataset (Rayner et al. 2003; Fig. 1a). The

TABLE 2. Spatial correlation coefficients for the modeled and observed Southern Hemisphere sea surface temperature difference, 1950 − 2000, and precipitation minus evaporation difference, 1960 − 2000, for the region north of 70°S and including the MMM. The models are compared to reanalysis products from HadISST for SST and both the NCEP-R1 (Kalnay et al. 1996) and the ERA-40 [Computational and Information Systems Laboratory (CISL) Research Data Archive, available online at http://dss.ucar.edu/; Kållberg et al. 2004] for $P - E$. Polar latitudes have been omitted from the correlation calculations because of large differences between the models biasing the coefficients. The correlation coefficient is defined as the covariance of the two datasets divided by the product of the standard deviation of the two datasets.

Model	SST	$P - E$ (NCEP-R1)	$P - E$ (ERA-40)
CGCM3.1	0.42	−0.044	0.051
CSIRO Mk3.0	0.21	−0.064	−0.024
CSIRO Mk3.5	0.21	0.045	0.089
ECHO-G	0.29	0.033	0.12
GISS-ER	0.32	0.024	0.18
HadCM3	0.053	−0.16	−0.016
MIROC(medres)	0.12	0.15	−0.054
GFDL CM2.1	0.24	−0.061	0.0080
MMM	0.40	−0.052	0.094

observed warming was strongest in the Indian Ocean and in small regions off the northwest and southeast coasts of South America. The SST decreased in some high-latitude regions, in the southwest Pacific Ocean, and in the west Atlantic Ocean. The spatial pattern of SST changes in the MMM (Fig. 1b) qualitatively agrees with the HadISST dataset over the same period, though the magnitude of the warming and cooling trends in the MMM are generally weaker (Fig. 1c), with the maximum change in the MMM SST being 0.7°C. The standard error of the MMM is small (<0.5°C, Fig. 1d), indicating a general consistency between the trends in the individual models.

The eight models (Figs. 1e–1l) reproduce warming trends north of about 45°S and cooling trends at high latitudes. However, only the ECHAM and the Meteorologischen Institut der Universität Bonn global Hamburg Ocean Primitive Equation (MIUB ECHO-G) model captures the cooling trend in the southwest Pacific Ocean. In ECHO-G and the Geophysical Fluid Dynamics Laboratory Climate Model version 2.1 (GFDL CM2.1), the cooling trend extends into the subtropics, as well as the regions of deep winter mixed layers, where SAMW and AAIW subduct strongly (see section 4). The difference in how well the models reproduce the observed SST trends have consequences for changes in the mixed layer depths and, therefore, for Southern Ocean water mass ventilation rates. We found the correlation between the HadISST and most of the CMIP3 models was ~0.3 (Table 2), with the MMM and Canadian Centre for Climate Modelling and Analysis (CCCMA) Coupled General Circulation Model, version 3.1 (CGCM3.1) showing the highest correlations (0.4 and 0.42, respectively).

Compared to the National Centers for Environmental Prediction–National Center for Atmospheric Research (NCEP–NCAR) Global Reanalysis 1 (NCEP-R1) and 40-yr European Centre for Medium-Range Weather Forecasts (ECMWF) Re-Analysis (ERA-40) products, all models are able to capture the observed increased evaporation in the tropics, decreased precipitation at midlatitudes, and increased freshening at high latitudes (Fig. 2). The spatial distribution of $P - E$ trends differs widely among the models, though the models are in rough agreement in the magnitude of the trends. However, the magnitude of the observed change in $P - E$ from the NCEP-1 and ERA-40 datasets (Figs. 2a and 2b) is higher than any of the models throughout the Southern Hemisphere. The standard error across the eight models (Fig. 2d) shows the greatest spread is found north of 35°S and along the Antarctic coast, with better agreement in regions of SAMW and AAIW formation. We found the modeled mean $P - E$ correlated well with NCEP-1 and ERA-40; however, the spatial correlations between the models and NCEP-1 and ERA-40 are low and inconsistent across the eight models (Table 2). In addition, the correlation between NCEP-R1 and ERA-40 is also low (0.14). Reasons for these low correlations are discussed later in this section.

A comparison of the mean 1981–2000 position of the zero wind stress curl is illustrated in Fig. 3. The spread between models is large, spanning more than 15° of latitude. The MMM (black solid curve) is biased slightly northward of observations (dashed curve; Rayner et al. 2003) in the Indian and Pacific Oceans. In the CGCM3.1, the zero wind stress curl line is significantly more equatorward than observed in each basin; the same is true for the Model for Interdisciplinary Research on Climate 3.2, medium-resolution version [MIROC(mderes)] in the Pacific. The position of the zero wind stress curl influences the spatial location of the deep winter mixed layers and, consequently, the regions of strong water mass subduction.

In summary, we find that despite substantial differences in some fields, the eight CMIP3 models are generally able to reproduce the large-scale trends of warming in the mid and low latitudes, cooling at high latitudes, and a southward shift and strengthening of the midlatitude precipitation band. In addition, the spread of results around the MMM contains useful information about model uncertainty and the value of the individual state variables. It is important to assess how these differences between models manifest themselves in subduction and changes in water mass formation, given that these models are the only tools we have to project future climate.

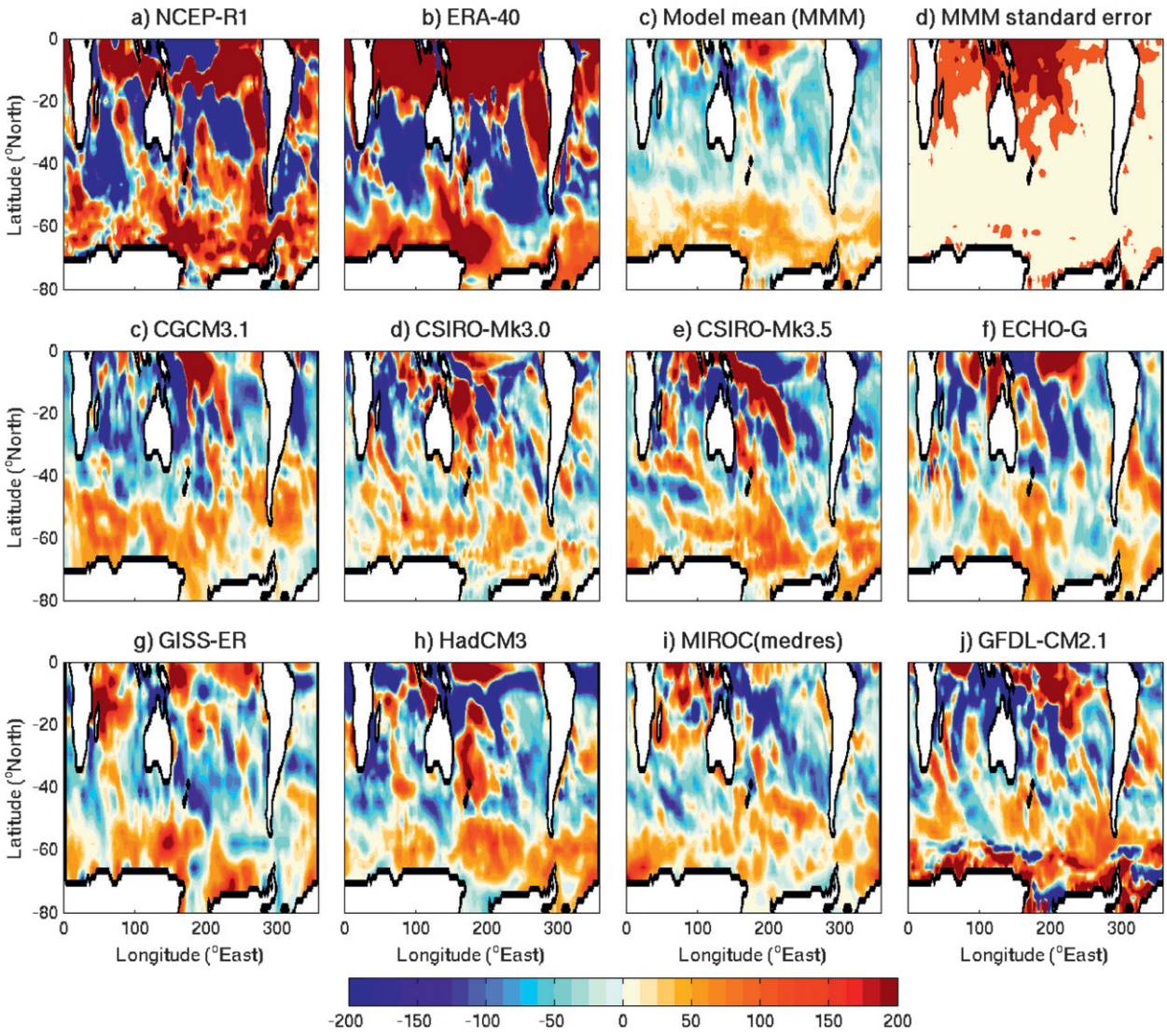

FIG. 2. Precipitation minus evaporation trend shown as the difference $P - E$ rate (mm yr^{-1}) for the period 1960–2000 in (a) NCEP-R1, (b) ERA-40, (c) the MMM, (d) the standard error in the MMM, and (e)–(l) the CMIP3 models.

There are two bias issues arising from results presented in this section. First, instrumental errors in the NCEP-R1 product (e.g., Marshall and Harangozo 2000; Bromwich and Fogt 2004), which have been found to contribute to inconsistencies when compared to IPCC models (Cai and Cowan 2007), may explain the large magnitude of the NCEP-R1 $P - E$ difference from 1950 to 2000. Second, the number of models and experiments assessed, as well as the type of dataset and the time period over which the models are assessed, may strongly influence the conclusions drawn regarding how well models can reproduce the observations. Many multimodel IPCC analyses (e.g., Russell et al. 2006; Fyfe and Saenko 2006; Sloyan and Kamenkovich 2007; Connolley and Bracegirdle 2007) (including our analysis) use a subset of the 23 IPCC AR4 models, which results in a different magnitude and sign for the model mean.

4. Results

a. Projected changes in the winter mixed layer depth

In the following we refer to the 1981–2000 period as "20C3M" and the projection period 2081–2100 as "A2." The subduction rate depends heavily on the slope of the mixed layer depth (WMLD) in the Southern Ocean, and the consequences of changes in the winter mixed layer depth changes are explored here. The 20C3M deepest winter mixed layers (i.e., the regions enclosed by the dashed 300-m contour in Fig. 4) correspond to SAMW and AAIW formation in the southeast Indian and Pacific

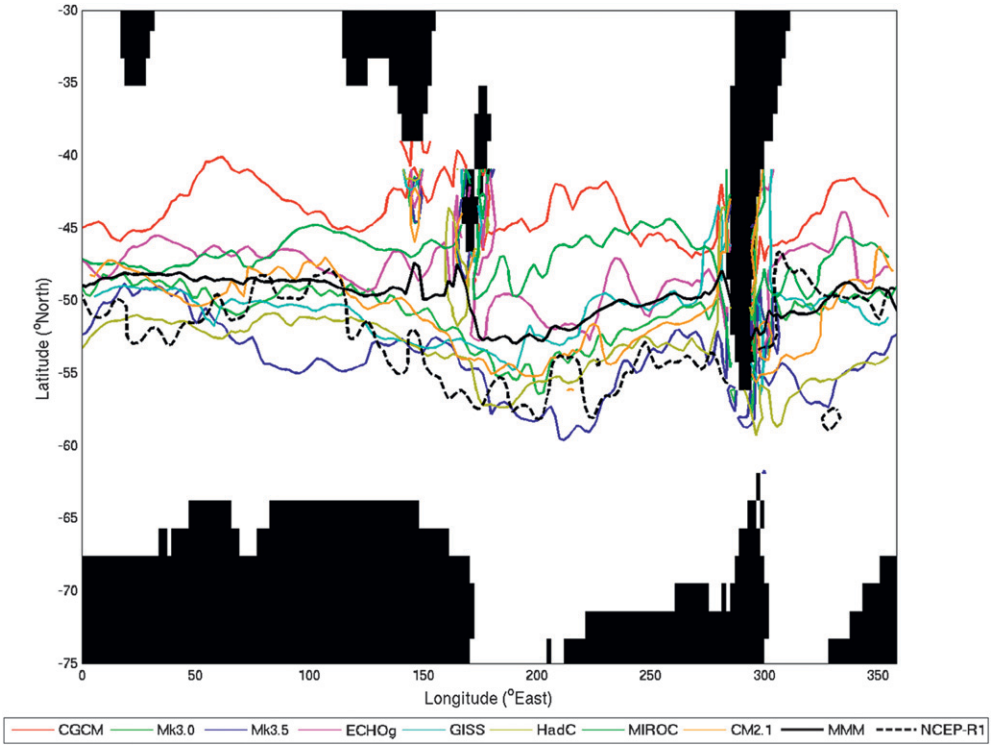

FIG. 3. Zero wind stress curl (Pa m^{-1}) for the 1981–2000 mean period. The MMM (black solid) and eight models (see legend for colors) are compared with the NCEP-R1 (black dashed).

basins. In most models (and hence the MMM), we find that the winter mixed layer depth falls in the observed range between 300 and 600 m (Sallée et al. 2006; Dong et al. 2008). The Commonwealth Scientific and Industrial Research Organisation Mark version 3.0 (CSIRO Mk3.0) and Goddard Institute for Space Studies Model E-R (GISS-ER) models produce the deepest WMLDs and tend to have cold and salty mode and intermediate waters. The third climate configuration of the Met Office Unified Model (HadCM3), with the freshest upper Southern Ocean, produces thin and shallow winter mixed layers. Some models show unrealistically deep mixed layers near Antarctica as a result of weak stratification. In the ECHO-G model, the small area for mode-water formation near 80°E is difficult to separate from deep mixed layers protruding from the Antarctic coast along a similar longitude. Further, in this model the deep mixed layers in the southeast Pacific Ocean in the same model are located around 60°S, which is much farther south than in the other models.

Projected warming and freshening at the ocean surface increase the stratification (and potential vorticity) at the base of the mixed layer and reduce the mixed layer depth between 40° and 60°S (Fig. 4). There are two important types of changes in the mixed layer depth. The first is the decrease in the winter mixed layer thickness in the SAMW and AAIW formation regions. In the southeast Indian Ocean, the models show winter mixed layer depth decreases by between 50 and 300 m in the SAMW region. As there is considerable spatial variability in the pattern of WMLD shoaling in the southeast Indian and Pacific Oceans, the multimodel change is only $O(50\ \text{m})$.

The second important change in the winter mixed layer depth is that in some models, the strongest changes are not aligned with the deepest mixed layers in the 20C3M period (represented by the bold contours in Fig. 4). For example, in HadCM3 (Fig. 4f), there is a 50-m decrease in the mixed layer in the southwest Pacific Ocean but negligible change in the southeast Pacific Ocean. The greatest mixed layer depth decreases occur on the equatorward side of the 20C3M deep mixed layer regions. Adjacent regions of strong increases and decreases indicate locations where the deep mixed layer region has shifted poleward [e.g., in the CGCM3.1, MIROC(medres) and CM2.1 models]. The relationship between these mixed layer changes and the projected subduction rates will be discussed later in the paper.

b. Projected changes in θ–S properties of SAMW and AAIW

Sloyan and Kamenkovich (2007) assessed the ability of eight models to produce the potential vorticity and salinity

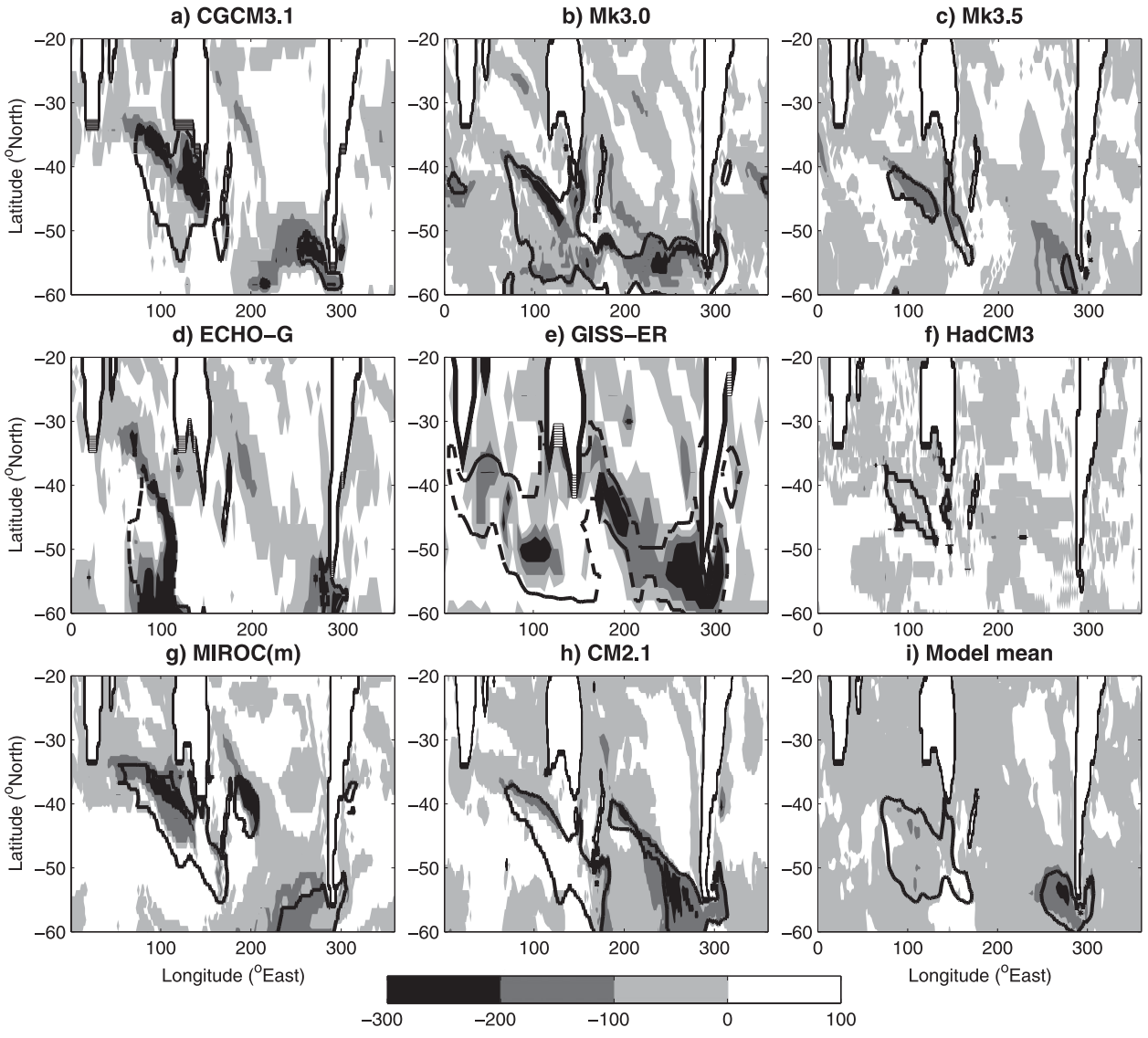

FIG. 4. Southern Ocean winter mixed layer depth (m) difference (A2 minus 20C3M, gray shading) with 20C3M winter mixed layer 300-m contour overlaid (black bold contours). The difference period used here is defined in the text. The MMM WMLD has been estimated by interpolating the models onto a 1° × 1° horizontal grid.

minimum on, and depth of, density surfaces using the CSIRO *Atlas of Regional Seas* 2006 climatology (available online at http://www.marine.csiro.au/~dunn/cars2006/). They found overall that the models were generally able to produce the low potential vorticity layer of SAMW and salinity minimum core of AAIW, but the models differed in the spatial distribution of these water masses and the depth and density at which they circulated northward. Here we assess the changes in the SAMW and AAIW temperature and salinity properties in density space.

Because the water mass densities evolve with time over the 100-yr analysis period, the density corresponding to SAMW and AAIW also changes with time. In addition, the same set of density classes for each basin and decade is not applied to all eight IPCC models because of differences in the density distribution between models. Here, the salinity and potential vorticity are interpolated onto neutral density surfaces, and the basin means are calculated for each decade. Following this, the low potential vorticity (referred to as PV_{low}) and salinity minimum (referred to as S_{min}), and the associated core densities, are determined. The mode and intermediate water mass layers are then defined as the core PV_{low} and S_{min} density ± 0.03 kg m^{-3}. The circumpolar average of θ–S curves for latitudes south of 32°S is shown in Fig. 5, and the circumpolar mean density range of SAMW and

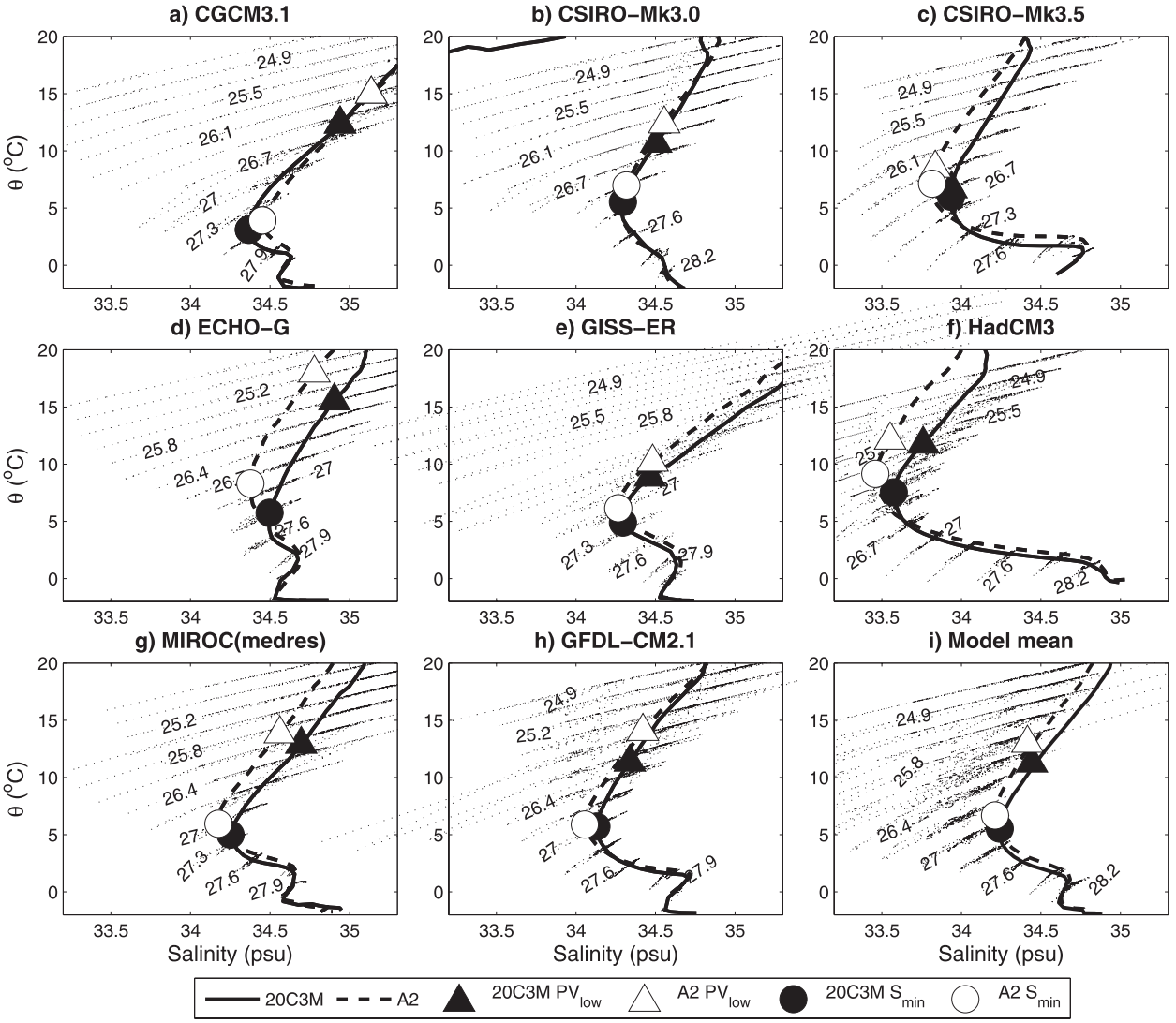

FIG. 5. Circumpolar average of θ–S curves in density space (kg m^{-3}; dotted curves) for the 20C3M models and period (solid line) and A2 models and period (dashed line). There is a 0.3 kg m^{-3} contour interval for the density surfaces. Overlaid on the plots are the core densities of SAMW (PV_{low}; triangle) and AAIW (S_{min}; circle) waters for the 20C3M control model and period (filled triangle) and A2 (unfilled triangle).

AAIW layers for each model is listed in Table 3. The symbols represent the core densities of SAMW (triangles) and AAIW (circles). The θ–S curves vary significantly across models. In the 20C3M, the models average temperature and salinity for SAMW for all basins range between 6.7° and 15.5°C and 33.9 and 34.9 psu, which mostly fall within the range of observed Southern Ocean θ and S ranges for SAMW (4°–15°C, 34.2–35.8 psu) (McCartney 1977; Hanawa and Talley 2001). The 20C3M model average AAIW temperature and salinity range between 3.1° and 7.5°C and 33.6 and 34.5 psu for the different models.

The projected θ–S changes are described first along the same density surfaces, followed by an analysis of the property changes for the SAMW and AAIW core densities. Despite the differences in the salinity minimum magnitude between models, all models indicate cooling and freshening of water on a given density surface for densities less than the salinity minimum density, as well as a shift in the θ–S curves to lighter density surfaces. This consistent cooling and freshening pattern is similar to the changes observed over the past 30–40 years (e.g., Johnson and Orsi 1997; Banks et al. 2002; Banks and Bindoff 2003; Bryden et al. 2003). There are some exceptions; the first is the CGCM3.1 climate model in the Pacific Ocean, where the projected θ–S curve, in the range γ^n = 27.4–27.7 kg m^{-3}, is entirely to the right of the mean twentieth-century climate, corresponding to warmer and more saline

TABLE 3. Water mass density classes for SAMW and AAIW for 1981–2000 (20C3M) and 2081–00 (A2). Units for the neutral density ranges are kg m^{-3}.

Model	SAMW 20C3M	SAMW A2	AAIW 20C3M	AAIW A2
CGCM3.1	26.2–26.8	25.8–26.4	27.1–27.7	27.1–27.7
CSIRO Mk3.0	26.2–26.8	25.9–26.5	26.9–27.5	26.7–27.3
CSIRO Mk3.5	26.4–27.0	26.0–26.6	26.5–27.1	26.3–26.9
MIUB ECHO-G	25.5–26.1	25.0–25.6	27.0–27.6	26.5–27.1
GISS-ER	26.4–27.0	26.2–26.8	26.9–27.5	26.7–27.3
HadCM3	25.5–25.9	25.0–25.6	25.9–26.5	25.5–26.1
MIROC(medres)	25.9–26.5	25.6–26.2	26.9–27.5	26.7–27.3
GFDL CM2.1	25.9–26.5	25.4–26.0	26.7–27.3	26.6–27.2
MMM	26.0–26.6	25.6–26.2	26.8–27.4	26.5–27.1

waters in both density and depth coordinates, due to large cooling between 55° and 65°S in the southwest Pacific basin (figure not shown). The CSIRO Mk3.0 model in the Atlantic Ocean shows little temperature change for densities less than 27.7 kg m^{-3}, and surface water masses are more saline on depth and density surfaces. The temperature and salinity properties of deep water are located between the salinity minimum and maximum (e.g., 27.3–27.9 kg m^{-3} for the MMM in Fig. 5). The models show an overall increase in the temperature and salinity for deep water. Aoki et al. (2005) noted that similar patterns found during the late twentieth century were due to the mixing of warmer and fresher surface waters.

In the 20C3M period, the simulated circumpolar depths of the SAMW (AAIW) density layers range between 200 and 750 m (500 and 1250 m) in the subtropical gyres. All models project deepening and a poleward shift of density surfaces, associated with the strengthening and poleward shift of the midlatitude westerlies. In addition, the cooling and freshening anomalies on density surfaces (see Fig. 5) correspond to a surface warming, as shown in Bindoff and McDougall (1994). All models project SAMW (triangles) and AAIW (circles) shift to lighter densities in the A2, except for the GISS-ER model in which SAMW remains at the same density (Fig. 5). Both SAMW and AAIW generally warm and freshen as they change density classes (AAIW is more saline in the CGCM3.1 and GISS-ER models in the A2). SAMW warms between 0.4° and 2.7°C and freshens between 0.02 and 0.2 psu; the corresponding range of changes for AAIW is 0.2° and 2.5°C, and 0.03 and 0.1 psu. There were a few exceptions to the overall salinity changes, the Mk3.0 and CGCM3.1 models projecting a more saline SAMW and AAIW, respectively.

c. Changes in the subduction of SAMW and AAIW

Using the water mass density class definitions above, SAMW and AAIW are assessed quantitatively to determine the subduction rate at the end of the twenty-first century. The lateral subduction term ($-\mathbf{u}_H \cdot \nabla H$) depends on the mixed layer depth slope and the horizontal velocities. In the SAMW and AAIW formation regions where the mixed layers are deep (and the mixed layer depth slope is large and positive), the lateral subduction term controls the total subduction rate. We also found that the projected changes in the subduction rate in the Southern Ocean are dominated by changes in this lateral term with a smaller contribution from changes in the vertical term.

For the eight models, the 20C3M basin-averaged annual mean subduction rates range between 30 and 175 m yr^{-1} for SAMW and between 30 and 250 m yr^{-1} for AAIW. These subduction rates fall within the observed range (Karstensen and Quadfasel 2002a). The maximum model subduction regions (greater than 150 m yr^{-1}) in the southeast Indian Ocean are located in the same region as the northern part of the deep winter mixed layers for SAMW formation. In the A2 projection, the subduction rate generally decreases where the 20C3M subduction rates are large and positive (i.e., permanent subduction into the ocean interior) and where the strongest decreases in the winter mixed layer depth occur (see Fig. 4).

The 20C3M and A2 subduction rates were converted into equivalent subduction transports (Figs. 6 and 7). Only the positive component of the subduction rate is used here because it is representative of fluid irreversibly entering the main thermocline. We found a large range in the net 20C3M subduction values among the models: from 30 to 114 Sv for SAMW and 19 to 102 Sv for AAIW. The subduction of AAIW in the CGCM3.1 model is considerably smaller than in the other models (Fig. 7) due to an equatorward zero wind stress curl (leading to upwelling in formation regions; Fig. 3) and a denser salinity minimum (hence the salinity minimum is located south of the maximum subduction regions; Fig. 5a). In the MMM, 63 Sv of SAMW and 60 Sv of AAIW is subducted; about half of this subduction occurs in the Pacific Ocean. Qu et al. (2008) and Karstensen and Quadfasel (2002a) estimated smaller volumes (~15 Sv) than the MMM (~25 Sv) for similar AAIW density ranges in the Pacific Ocean. We find that, overall, the models used here tend to subduct more fluid than observed.

Under the A2 scenario, subduction rates tend to decrease in each basin for both water masses, though the CGCM3.1 and CM2.1 (HadCM3) models project small increases for the SAMW (AAIW) class. In the MMM, the subduction of SAMW (Fig. 6) and AAIW (Fig. 7) decrease by 12% and 23%, respectively. The core density associated with these water masses also decreases, as discussed in the previous section. The projected changes in the winter mixed layer in the ECHO-G and CM2.1 models in the southeast Indian basin is weaker than in

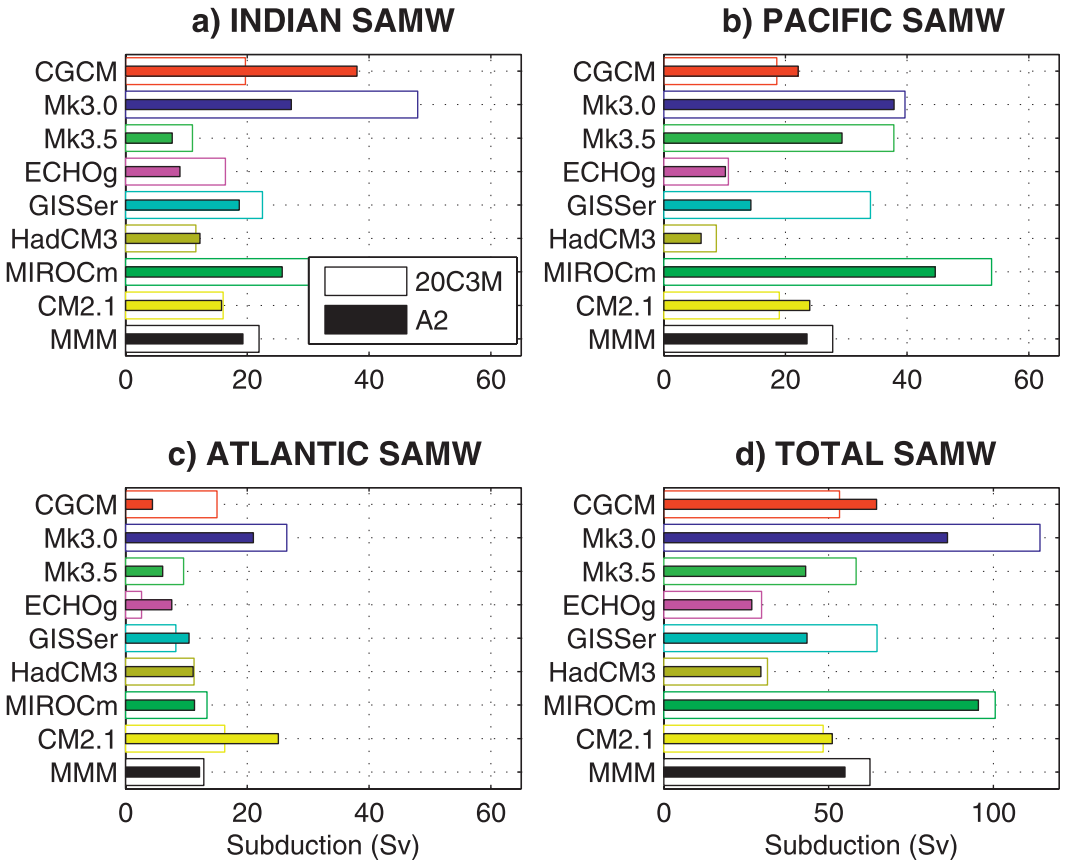

FIG. 6. The 20C3M (open bars) and A2 (colored bars) SAMW subduction transports (Sv) for the (a) Indian, (b) Pacific, and (c) Atlantic Oceans, and d) net SAMW subduction. The precise period for 20C3M and A2 models is defined in the text. The multi-model mean is denoted as MMM. The SAMW density class for each model is defined in Table 3.

other models (Fig. 4), and we found a cooling SST trend (1950 to 2000; Fig. 1) in these two models. The changes in surface temperature, and consequently the winter mixed layers, may account for the small changes (ECHO-G), or increases in (CM2.1), in the net subduction of SAMW in these models (Fig. 6d). Banks et al. (2002) (for the Indian Ocean) and Goes et al. (2008) (for the South Atlantic) concluded that changes in the SAMW density over time did not necessarily result in formation and subduction changes. We find a small change in the model mean subduction of SAMW in the Atlantic basin (1 Sv); however, there is a 14% decrease in the model mean in the Indian Ocean. To summarize, the models suggest SAMW and AAIW will both shift to lighter density classes and the subduction rate will decrease.

d. Surface buoyancy fluxes in the SAMW and AAIW formation regions

In this section we determine the surface buoyancy fluxes that contribute to the formation of SAMW and AAIW and the changes in their properties in the A2 projection. The contribution of the two major components in the annual mean net surface buoyancy flux [$\mathbf{B}_{in}$ and $\mathbf{B}_{Ek}$, Eq. (3)] to the formation of SAMW and AAIW in each basin are shown in Fig. 8, using the low potential vorticity and salinity minimum density classes for each model. Positive annual mean air–sea fluxes ($\mathbf{B}_{in}$) result from a surface buoyancy gain in the warmer months, outweighing the buoyancy loss in the wintertime, such as in the zonal mean 20C3M $\mathbf{B}_{in}$ over the SAMW outcrop in most models (Fig. 8a). In agreement with previous studies (Rintoul and England 2002; Speer et al. 2000; Saenko 2007), we find the MMM northward Ekman transport of cold waters into the SAMW formation region in the southeast Indian Ocean ($\mathbf{B}_{Ek}$, -16.3×10^{-6} kg m^{-1} s^{-3}; Fig. 8a) is larger than the surface warming at the SAMW outcrop. SAMW overlaps the zero wind stress curl in the Pacific and Atlantic basins; hence, the buoyancy acquired from the northward Ekman flux is minimal. Overall, AAIW lies south of the wind stress curl, in the upwelling zone ($\mathbf{B}_{Ek}$ positive), which weakens the mixed layer stratification (Dong et al. 2008), and this

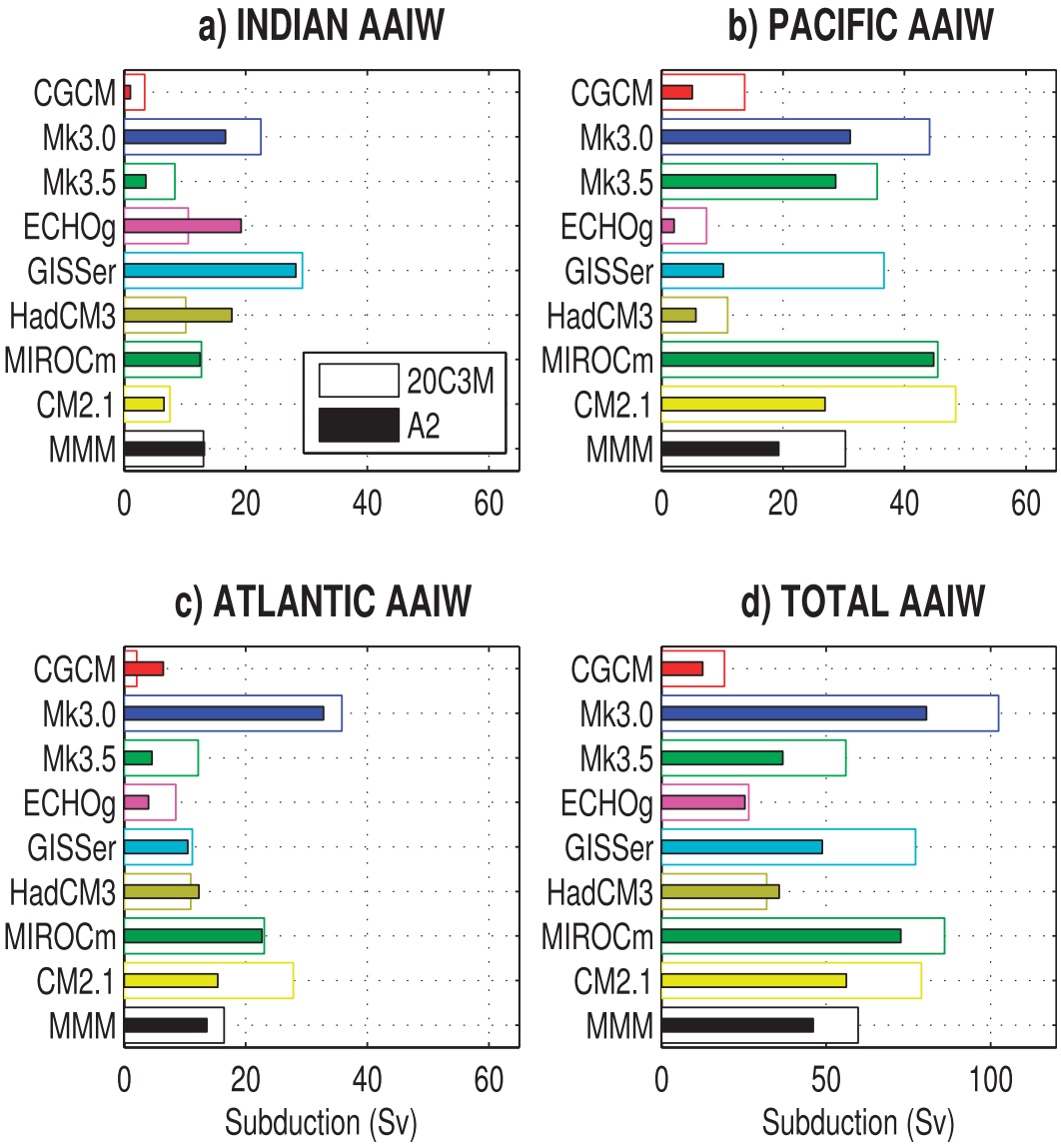

FIG. 7. As in Fig. 6, but for the net AAIW subduction.

feature of AAIW formation is reproduced by most of the IPCC models in Fig. 8b (circles).

Despite the significant spread of the models' 20C3M buoyancy fluxes, the models agree with the direction of the projected SAMW and AAIW buoyancy gain (Fig. 8; open shapes). The projected SAMW and AAIW buoyancy gain is due to changes in the air–sea fluxes rather than from the wind stress changes over the 100 years. There are increases in the northward transport of buoyancy in the Ekman layer for SAMW in the Indian Ocean and zonal average (shown by negative values; circles, Fig. 8a), corresponding to the modeled strengthening of the westerlies. However, the increases in the air–sea fluxes ($\mathbf{B}_{in}$) as SAMW and AAIW shift to lighter densities in the A2 exceed the changes in the Ekman transport of buoyancy. Both the air–sea fluxes contribute to the air–sea buoyancy flux. We find that in the 20C3M and A2 both the heat and freshwater fluxes play a strong role in the formation of SAMW and AAIW; however, it is the increased surface heat flux that dominates the projected increases in the net surface buoyancy fluxes (figure not shown).

5. Discussion and conclusions

We have examined the ability of eight IPCC models to capture observed changes in the surface fluxes and the properties of SAMW and AAIW on density surfaces.

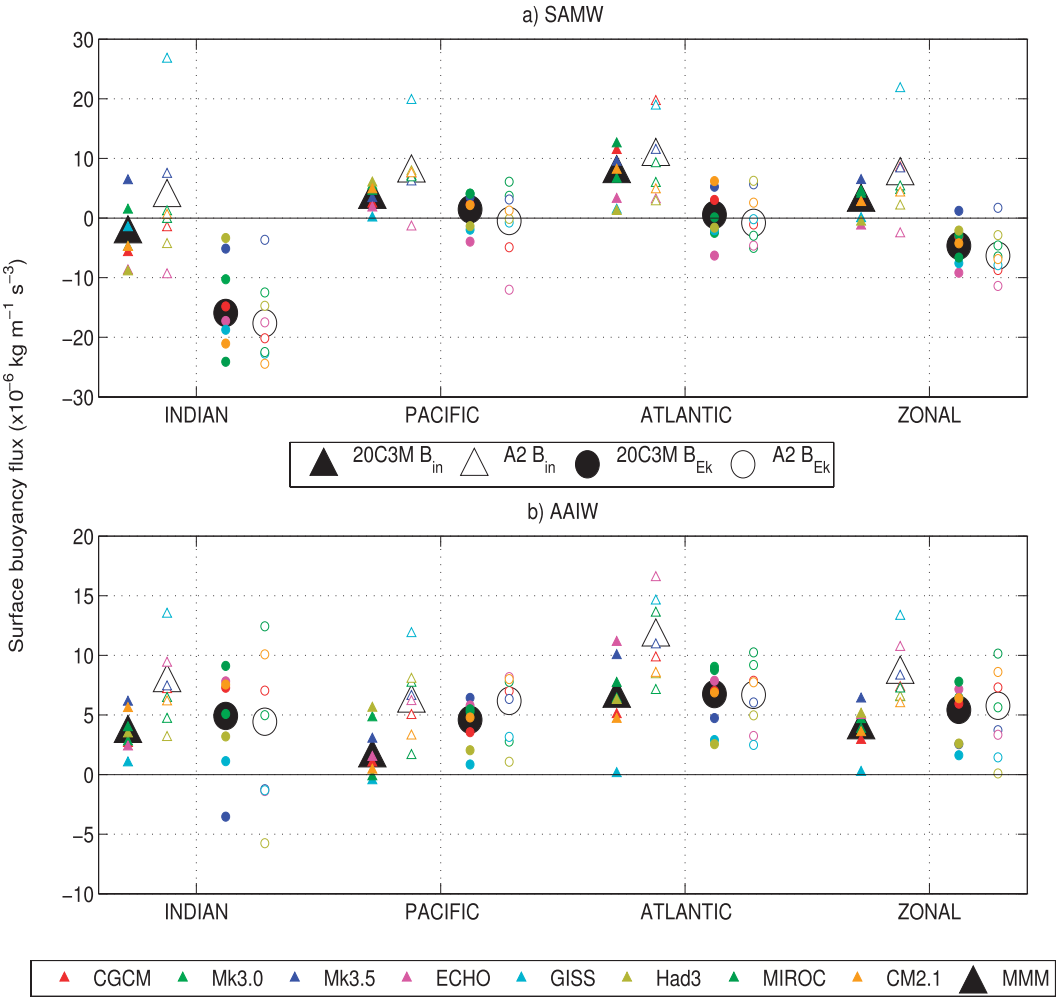

FIG. 8. The MMM surface buoyancy flux components averaged over the Indian, Pacific, and Atlantic Oceans, and the circumpolar average for (a) SAMW and (b) AAIW. The periods are 1981 to 2000 (20C3M; colored shapes) and 2081 to 2100 (A2; open shapes). The two components in each plot are the buoyancy into the ocean surface (heat flux and freshwater flux; B_{in}; triangles) and the buoyancy acquired through the Ekman flux of heat and freshwater (B_{Ek}; circles). Units for each term are $\times 10^{-6}$ kg m^{-1} s^{-3}. In each basin, SAMW is defined by the layer around the minimum in potential vorticity, and AAIW by the layer around the salinity minimum. Note that the net surface buoyancy flux equals $B_{in} - B_{Ek}$. The multi-model mean estimates are represented by the large triangles and circles (filled for 20C3M period, open for A2 period), and the eight models by the smaller shapes with respective colors indicated in the bottom legend.

Overall, the eight IPCC models and MMM are able to produce the observed sign and pattern of the changes in SST, $P - E$, and wind stress. However, the magnitude and distribution of regional changes and the associated densities differ between models. Over the 1950–2000 period, most of the Southern Hemisphere SST warmed by up to 1.1°C, and the greatest temperature increases were found in the equatorial region and the southeast Pacific, Atlantic, and south Indian regions (Fig. 1). Cooling (less than 0.8°C) was observed at high latitudes, and most of the models reproduce this cooling trend. There were large increases in the NCEP-R1 and ERA-40 $P - E$ rate (>300 m yr^{-1}) in some locations, with precipitation increasing at high latitudes and evaporation increasing north of 50°S (Fig. 2). We note that the models excluding ozone-depletion forcing (CGCM3.1 and ECHO-G) are not necessarily worse at simulating observed changes, in agreement with the conclusions drawn by Alory et al. (2007).

Our multimodel analysis is unique in that it quantifies the changes in the subduction of SAMW and AAIW and in the Southern Ocean interior, projected by IPCC models. The density field evolves through time, meaning that a particular water mass does not remain on the same isopycnal. The basin-verage densities corresponding to

the low potential vorticity, and salinity minimum layers were used to define SAMW and AAIW in each of the models in the 20C3M and A2 periods (Table 3). Most models project warming and freshening for SAMW and AAIW as they migrate to lighter density classes in the A2 period (Fig. 5). The projected warming and freshening of SAMW (AAIW) ranged between 0.4° and 2.7°C and 0.02 and 0.2 psu (0.2°–2.5°C and 0.03–0.1 psu). The poleward shift in the wind stress, and warming and freshening at the ocean surface, cause a southward shift in the density outcrop of water masses. We find the density surfaces deepen near the outcrop location and then shoal north of the midlatitudes.

The projected buoyancy gain, due to an increase in surface warming and freshening throughout the Southern Ocean (Fig. 8), results in stronger stratification and shallower winter mixed layers in the primary formation regions (SAMW: southeast Indian Ocean; AAIW: southeast Pacific Ocean). In the interior, the projected surface warming and freshening correspond to cooling and freshening on density surfaces, and these changes are similar to the patterns observed over the past few decades. There is a consistent model projection of a decrease in the subduction of SAMW (5%–26%) and AAIW (4%–37%). Lateral induction (1) makes the dominant contribution to both the mean subduction in the 20C3M period (in agreement with Karstensen and Quadfasel 2002b) and to the projected changes in the A2 scenario. However, the relative contribution of the lateral and vertical mechanisms varies between the 20C3M and A2 periods as the water mass properties evolve.

Both air–sea heat and freshwater fluxes and Ekman transport can drive changes in the buoyancy budget of the mixed layer and, hence, water mass formation. Rintoul and England (2002) concluded from repeat hydrographic observations and results from a coarse-resolution ocean model that Ekman transport of heat and freshwater played the dominant role in driving variations in θ and S properties in the SAMW formation regions. On the other hand, Banks and Bindoff (2003) and Murray et al. (2007) concluded from observations and model simulations in the ocean interior that variability in SAMW properties primarily reflected changes in surface heat and freshwater fluxes. Surface freshening (and to a lesser degree, cooling) have been observed as the main forcing responsible for AAIW formation in the southeast Pacific Ocean (Bindoff and McDougall 1994; Johnson and Orsi 1997; Wong et al. 1999; Banks and Bindoff 2003). In the models considered here, the formation of SAMW in the Indian Ocean is driven primarily by the Ekman flux of heat and freshwater, while in the other basins it is primarily driven by air–sea fluxes of heat and freshwater. Further, we found that the air–sea fluxes (primarily of heat) increase in the A2 projection, driving a buoyancy gain over the SAMW and AAIW outcrop regions.

The changes in the winter mixed layer, the temperature and salinity properties, and the subduction of water masses vary between models. Changes in subduction are influenced by the upper-ocean temperature and salinity fields, as well as the magnitude of the density shift in the A2 for SAMW and AAIW. For example, the HadCM3 model has a lighter surface density and shallower winter mixed layer (see Fig. 4), resulting in smaller SAMW and AAIW subduction rates in the 20C3M (Figs. 6 and 7). The models also differ with regard to flux adjustments, ozone inclusion, and model drift, which can affect their projections. For example, the CGCM3.1 and ECHO-G models include flux adjustments (heat and freshwater) and exclude ozone depletion forcing. These two models produced SAMW and AAIW north of the zero wind stress curl and had weaker subduction of AAIW in the 20C3M period (Fig. 7). Finally, the vertical velocity in HadCM3 and ECHO-G [approximated using Eq. (2)] is smaller than the other six models, which likely reduces the net subduction of SAMW and AAIW in these two models.

Despite the substantial differences between models and the varying success with which they reproduce late twentieth-century climate, the models show a consistent response of SAMW and AAIW formation to climate change in the twenty-first century. The projected warming and increased precipitation at the ocean surface strengthen the stratification at the mixed layer base and lead to a shoaling of the winter mixed layer. The surface changes result in cooling and freshening on density surfaces and a reduction in the subduction rate. The projected decrease of the flux of SAMW and AAIW into the main thermocline implies a likely reduction in the capacity of the Southern Ocean to sequester carbon in the future.

Acknowledgments. This work is supported by the Australian Government's Cooperative Research Centres program through the Antarctic Climate and Ecosystems CRC, by the CSIRO Wealth from Oceans National Research Flagship and the Australian Climate Change Science Program. We greatly appreciate the discussions on the theory of neutrals surfaces with Trevor McDougall and David Jackett and would like to express our thanks to Glenn Hyland, Martin Dix, and Joseph Majkut for their assistance with data access. We acknowledge the modeling groups for providing their data for analysis, the Program for Climate Model Diagnosis and Intercomparison (PCMDI) for collecting and archiving the model output, and the JSC/CLIVAR Working Group on Coupled Modelling (WGCM) for organizing

the model data analysis activity. The multimodel data archive is supported by the Office of Science, U.S. Department of Energy.

REFERENCES

Alory, G., S. Wijffels, and G. Meyers, 2007: Observed temperature trends in the Indian Ocean over 1960–1999 and associated mechanisms. *Geophys. Res. Lett.,* **34,** L02606, doi:10.1029/2006GL028044.

Aoki, S., N. L. Bindoff, and J. A. Church, 2005: Interdecadal water mass changes in the Southern Ocean between 30°E and 160°E. *Geophys. Res. Lett.,* **32,** L07607, doi:10.1029/2004GL022220.

Arguez, A., H. J. Diamond, F. Fetterer, A. Horvitz, and J. M. Levy, 2007: State of the climate in 2006. *Bull. Amer. Meteor. Soc.,* **88,** S1–S135.

Banks, H. T., and N. L. Bindoff, 2003: Comparison of observed temperature and salinity changes in the Indo-Pacific with results from the coupled climate model HadCM3: Processes and mechanisms. *J. Climate,* **16,** 156–166.

——, R. Wood, and J. Gregory, 2002: Changes to Indian Ocean Subantarctic Mode Water in a coupled climate model as CO_2 forcing increases. *J. Phys. Oceanogr.,* **32,** 2816–2827.

Bindoff, N. L., and T. J. McDougall, 1994: Diagnosing climate change and ocean ventilation using hydrographic data. *J. Phys. Oceanogr.,* **24,** 1137–1152.

Bromwich, D. H., and R. L. Fogt, 2004: Strong trends in the skill of the ERA-40 and NCEP–NCAR reanalyses in the high and midlatitudes of the Southern Hemisphere, 1958–2001. *J. Climate,* **17,** 4603–4619.

Bryden, H. L., E. L. McDonagh, and B. A. King, 2003: Changes in ocean water mass properties: Oscillations or trends? *Science,* **300,** 2086–2088.

Cai, W., and T. Cowan, 2007: Trends in Southern Hemisphere circulation in IPCC AR4 models over 1950–99: Ozone depletion versus greenhouse forcing. *J. Climate,* **20,** 681–693.

Connolley, W. M., and T. J. Bracegirdle, 2007: An Antarctic assessment of IPCC AR4 coupled models. *Geophys. Res. Lett.,* **34,** L22505, doi:10.1029/2007GL031648.

Covey, C., P. J. Gleckler, T. J. Phillips, and D. C. Bader, 2006: Secular trends and climate drift in coupled ocean–atmosphere general circulation models. *J. Geophys. Res.,* **111,** D03107, doi:10.1029/2005JD006009.

de Boyer Montégut, C., G. Madec, A. S. Fischer, A. Lazar, and D. Iudicone, 2004: Mixed layer depth over the global ocean: An examination of profile data and a profile-based climatology. *J. Geophys. Res.,* **109,** CL2003, doi:10.1029/2004JC002378.

Dirmeyer, P. A., 2001: Climate drift in a coupled land–atmosphere model. *J. Hydrometeor.,* **2,** 89–100.

Dong, S., J. Sprintall, S. T. Gille, and L. Talley, 2008: Southern Ocean mixed-layer depth from Argo float profiles. *J. Geophys. Res.,* **113,** C06013, doi:10.1029/2006JC004051.

Fyfe, J. C., and O. A. Saenko, 2006: Simulated changes in the extratropical Southern Hemisphere winds and currents. *Geophys. Res. Lett.,* **33,** L06701, doi:10.1029/2005GL025332.

Goes, M., I. Wainer, P. R. Gent, and F. O. Bryan, 2008: Changes in subduction in the South Atlantic Ocean during the 21st century in the CCSM3. *Geophys. Res. Lett.,* **35,** L06701, doi:10.1029/2007GL032762.

Hanawa, K., and L. D. Talley, 2001: Mode waters. *Ocean Circulation and Climate,* G. Siedler, J. Church, and J. Gould, Eds., Academic Press, 373–386.

Huang, R. X., and B. Qiu, 1998: The structure of the wind-driven circulation in the subtropical South Pacific Ocean. *J. Phys. Oceanogr.,* **28,** 1173–1186.

Johnson, G. C., and A. H. Orsi, 1997: Southwest Pacific Ocean water-mass changes between 1968/69 and 1990/91. *J. Climate,* **10,** 306–316.

Kållberg, P., A. Simmons, S. Uppala, and M. Fuentes, 2004: The ERA-40 archive. ERA-40 Project Tech. Rep. 17, ECMWF, 31 pp.

Kalnay, E., and Coauthors, 1996: The NCEP/NCAR 40-Year Reanalysis Project. *Bull. Amer. Meteor. Soc.,* **77,** 437–471.

Karstensen, J., and D. Quadfasel, 2002a: Formation of Southern Hemisphere thermocline waters: Water mass conversion and subduction. *J. Phys. Oceanogr.,* **32,** 3020–3038.

——, and ——, 2002b: Water subducted into the Indian Ocean subtropical gyre. *Deep-Sea Res. II,* **49,** 1441–1457.

Levitus, S., 1982: *Climatological Atlas of the World Ocean*. NOAA Prof. Paper 13, 173 pp. and 17 microfiche.

Marshall, G. J., and S. A. Harangozo, 2000: An appraisal of NCEP/NCAR reanalysis MSLP data viability for climate studies in the South Pacific. *Geophys. Res. Lett.,* **27,** 3057–3060.

Marshall, J. C., A. J. G. Nurser, and R. G. Williams, 1993: Inferring the subduction rate and period over the North Atlantic. *J. Phys. Oceanogr.,* **23,** 1315–1329.

McCartney, M. S., 1977: Subantarctic Mode Water. *A Voyage of Discovery: George Deacon 70th Anniversary Volume,* M. V. Angel, Ed., Pergamon, 103–119.

McNeil, B. I., R. J. Matear, R. M. Key, J. L. Bullister, and J. L. Sarmiento, 2003: Anthropogenic CO_2 uptake by the ocean based on the global chlorofluorocarbon data set. *Science,* **299,** 235–239.

Meehl, G., and Coauthors, 2009: IPCC standard output from coupled ocean-atmosphere GCMs. WGCM Climate Simulation Panel/PCMDI Rep., 33 pp. [Available online at http://www-pcmdi.llnl.gov/ipcc/standard_output.pdf.]

Murray, R. J., N. L. Bindoff, and C. J. C. Reason, 2007: Modeling decadal changes on the Indian Ocean section I5 at 32°S. *J. Climate,* **20,** 3106–3130.

Naveira-Garabato, A. C., J. T. Allen, H. Leach, V. H. Strass, and R. T. Pollard, 2001: Mesoscale subduction at the Antarctic Polar Front driven by baroclinic instability. *J. Phys. Oceanogr.,* **31,** 2087–2107.

Nurser, A. J. G., R. Marsh, and R. G. Williams, 1999: Diagnosing water mass formation from air–sea fluxes and surface mixing. *J. Phys. Oceanogr.,* **29,** 1468–1487.

Orr, J. C., and Coauthors, 2001: Estimates of anthropogenic carbon uptake from four three-dimensional global ocean models. *Global Biogeochem. Cycles,* **15,** 43–60.

Qiu, B., and R. X. Huang, 1995: Ventilation of the North Atlantic and North Pacific: subduction versus obduction. *J. Phys. Oceanogr.,* **25,** 2374–2390.

Qu, T., S. Gao, I. Fukumori, R. A. Fine, and E. J. Lindstrom, 2008: Subduction of South Pacific waters. *Geophys. Res. Lett.,* **35,** L02610, doi:10.1029/2007GL032605.

Rahmstorf, S., 1995: Climate drift in an ocean model coupled to a simple, perfectly matched atmosphere. *Climate Dyn.,* **11,** 447–458.

Randall, D. A., and Coauthors, 2007: Climate models and their evaluation. *Climate Change 2007: The Physical Science Basis,* S. Solomon et al., Eds., Cambridge University Press, 589–662.

Raphael, M. N., and M. M. Holland, 2006: Twentieth century simulation of the Southern Hemisphere climate in coupled models. Part I: Large scale circulation variability. *Climate Dyn.,* **26,** 217–228.

Rayner, N. A., D. Parker, E. B. Horton, C. K. Folland, L. V. Alexander, D. P. Rowell, E. C. Kent, and A. Kaplan, 2003: Global analyses of sea surface temperature, sea ice, and night marine air temperature since the late nineteenth century. *J. Geophys. Res.,* **108,** 4407, doi:10.1029/2002JD002670.

Reichler, T., and J. Kim, 2008: How well do coupled climate models simulate today's climate? *Bull. Amer. Meteor. Soc.,* **89,** 303–311.

Rintoul, S. R., and M. H. England, 2002: Ekman transport dominates local air–sea fluxes in driving variability of Subantarctic Mode Water. *J. Phys. Oceanogr.,* **32,** 1308–1321.

Russell, J. L., R. J. Stouffer, and K. W. Dixon, 2006: Intercomparison of the Southern Ocean circulations in IPCC coupled model control simulations. *J. Climate,* **19,** 4560–4575.

Sabine, C. L., R. M. Key, K. M. Johnson, F. J. Millero, A. Poisson, J. L. Sarmiento, D. W. R. Wallace, and C. D. Winn, 1999: Anthropogenic CO_2 inventory of the Indian Ocean. *Global Biogeochem. Cycles,* **13,** 179–198.

——, and Coauthors, 2004: The oceanic sink for anthropogenic CO_2. *Science,* **305,** 367–371.

Saenko, O. A., 2007: Ocean circulation: Mechanisms and impacts. *Projected Strengthening of the Southern Ocean Winds: Some Implications for the Deep Ocean Circulation, Geophys. Monogr.,* Vol. 173, Amer. Geophys. Union, 365–382.

Sallée, J.-B., N. Wienders, K. Speer, and R. Morrow, 2006: Formation of Subantarctic Mode Water in the southeastern Indian Ocean. *Ocean Dyn.,* **56,** 525–542.

——, K. Speer, S. R. Rintoul, and S. Wijiffels, 2010: Southern Ocean thermocline ventilation. *J. Phys. Oceanogr.,* **40,** 509–529.

Sen Gupta, A., A. Santoso, A. S. Taschetto, C. C. Ummenhofer, J. Trevena, and M. H. England, 2009: Projected changes to the Southern Hemisphere ocean and sea ice in the IPCC AR4 climate models. *J. Climate,* **22,** 3047–3078.

Sloyan, B. M., and I. V. Kamenkovich, 2007: Simulation of Subantarctic Mode Water and Antarctic Intermediate Water in climate models. *J. Climate,* **20,** 5061–5080.

Solomon, S., D. Qin, M. Manning, M. Marquis, K. Averyt, M. M. B. Tignor, H. L. Miller Jr., and Z. Chen, 2007: *Climate Change 2007: The Physical Science Basis*. Cambridge University Press, 996 pp.

Speer, K., S. R. Rintoul, and B. Sloyan, 2000: The diabatic Deacon cell. *J. Phys. Oceanogr.,* **30,** 3212–3222.

Speich, S., and Coauthors, 2004: Southern Ocean chokepoints: Monitoring fluxes associated with water exchanges between the three ocean basins. CLIVAR Rep., 11 pp. [Available online at http://www.clivar.org/organization/southern/documents/Chokepoints_IPY.pdf.]

Takahashi, T., and Coauthors, 2002: Global sea-air CO_2 flux based on climatological surface ocean pCO_2, and seasonal biological and temperature effects. *Deep-Sea Res. II,* **49,** 1601–1623.

Wong, A. P. S., N. L. Bindoff, and J. A. Church, 1999: Large-scale freshening of intermediate waters in the Pacific and Indian Oceans. *Nature,* **400,** 440–443.